chemosensors

MDPI

Article

Potentiometric C_2H_4-Selective Detection on Solid-State Sensors Activated with Bifunctional Catalytic Nanoparticles

Fidel Toldra-Reig and Jose Manuel Serra *

Instituto de Tecnología Química, Universitat Politècnica de València, Consejo Superior de Investigaciones Cientèficas, Av Naranjos s/n, E-46022 Valencia, Spain; fitolrei@itq.upv.es
* Correspondence: jmserra@itq.upv.es

Abstract: This work presents a solid-state ionic-based device to selectively detect C_2H_4 in car exhaust gases. The sensor consists of 8YSZ as the electrolyte and two electrodes: $Fe_{0.7}Cr_{1.3}O_3$/8YSZ and LSM/8YSZ. The main aim of this work is to optimize the catalytic behavior of the working electrode to C_2H_4 and reduce cross-sensitivity toward CO and H_2O. Several catalyst nanoparticles were infiltrated to tailor C_2H_4 adsorption and electrochemical oxidation properties while diminishing adsorption and conversion of other gas components such as CO. The infiltrated metal catalysts were selected, taking into account both adsorption and redox properties. Infiltration of Ti or Al, followed by a second infiltration of Ni, enabled the selective detection of C_2H_4 with low cross-sensitivity toward CO and H_2O in a moist gas environment. Further insight into potentiometric C_2H_4 sensing is achieved by electrochemical impedance analysis of the electrodes activated with bifunctional catalysts.

Keywords: hydrocarbon; ethylene; potentiometric; sensor; catalysis

Citation: Toldra-Reig, F.; Serra, J.M. Potentiometric C_2H_4-Selective Detection on Solid-State Sensors Activated with Bifunctional Catalytic Nanoparticles. *Chemosensors* **2021**, *9*, 274. https://doi.org/10.3390/chemosensors9100274

Academic Editors: Valerio Vignoli and Enza Panzardi

Received: 31 July 2021
Accepted: 22 September 2021
Published: 27 September 2021

1. Introduction

Currently, the public health factor involving pollution in cities is a hot topic [1–3]. Legislation is becoming more restrictive with regard to both polluting emissions from road vehicles and car circulation in the innermost part of cities. This involves both existing and future automotive fleets and better monitoring of environmental performance (defeat devices, tampered antipollution systems, etc.). This is a concern for the European Commission, and it has been included in their work programs for smart, green integrated transport in H2020 during the 2018–2020 period. This is also tackled in the Horizon Europe work program for Climate, Energy, and Mobility for 2021–2022 [4]. Among different actions, pollution tolls and further emission controls are under consideration in cities to ban the most polluting cars within urban areas [5–9]. Therefore, more restrictive legislation is expected in the short term. However, legislators cannot lower emission limits because of the current lack of devices able to detect low contents of hydrocarbons selectively. Therefore, the availability of an economically attractive, reliable, and highly sensitive hydrocarbon sensor could help to establish this sensor in combustion engines but also in the monitoring of gas streams in other combustion or thermochemical processes.

The elevated temperature of exhaust gases and exhaust gas content make potentiometric sensors the most appealing option. In the literature, zirconia and platinum are widely employed as electrolyte and reference electrodes, respectively [10–17]. As working electrodes, different oxides, from simple to more complex oxides [12,17–21] such as spinels and perovskites, are used for the detection of several elements, e.g., hydrocarbons [10,15,22–26], CO [19,27–29], and NH_3 [30,31]. The general problem is not only the use of expensive noble metals but also poor selectivity to the target gas and/or high cross-sensitivity toward other elements. Responses to single gases are compared without comparing the effect of other gases in a gas mixture as expected in real applications. In this work, a potentiometric hydrocarbon sensor is optimized by surface functionalization of its working electrode [32,33], avoiding the use of noble metals to enhance selectivity

to ethylene. It consists of a solid ionic electrolyte (8YSZ) and two electrodes: LSM/8YSZ as the reference electrode and $Fe_{0.7}Cr_{1.3}O_3$/8YSZ as the working electrode. Additionally, both electrodes are exposed to the same atmosphere. This simplifies the device and allows it to behave according to the mixed-potential theory, i.e., several reduction and oxidation reactions running simultaneously at each electrode, where one controls the kinetics. When equilibrium is achieved in each electrode, a difference in voltage that can be measured is generated [13,34–36]. Therefore, reference and working electrodes must be selective to an oxygen cathodic reaction and to a target gas anodic reaction, respectively. Kinetics in each electrode must be controlled by these reactions. C_2H_4 is a major hydrocarbon in exhaust gas [37–40]; therefore, it is considered a target gas. Additionally, cross-sensitivity toward any elements common in exhaust gas such as CO, H_2O, and polyaromatics ($C_{11}H_{10}$ and $C_{14}H_{10}$) should be kept low during dynamic operation.

This work focuses on the catalytic functionalization of the working electrode (WE) in order to provide a specific response to C_2H_4 with low cross-sensitivity against CO and H_2O, i.e., fostering C_2H_4 electrochemical oxidation kinetics. This is accomplished by means of electrode infiltration with distinct nanosized catalysts. The device consists of a common reference electrode on one face of the solid electrolyte and four different working electrodes on the other face of the electrolyte. Nickel dispersion on the WE has been reported to boost electrochemical C_2H_4 oxidation [41]. Several catalytic materials are selected in this work because of their redox activity or adsorption properties related to hydrocarbons and CO: Al [42], Ti [43], Ni [41,44], Ru [45–47], Pd [48,49], Nb [50], and Ba. Some of these specific elements were selected because of their Lewis acidity or basicity (for the alkali elements) of related cationic species [48].

Thus, several nanosized catalysts, including binary combinations, are incorporated in the sensor WE to selectively improve electrochemical C_2H_4 oxidation. The open-circuit voltage generated between both electrodes is measured for concentration pulses of C_2H_4 and CO in both dry and humidified conditions. Moreover, electrochemical impedance spectroscopy is carried out for a better understanding of the processes taking place at the activated electrodes.

2. Experimental

2.1. Sample Preparation

Both $La_{0.9}Sr_{0.1}MnO_3$ perovskite (LSM) and $Fe_{0.7}Cr_{1.3}O_3$ were synthesized by means of a sol–gel chemical route. Commercial nitrates from Sigma-Aldrich were used as precursors. Citric acid (Sigma-Aldrich, St. Louis, MO, USA) was added to the stoichiometric water-based solution to prevent partial segregation of the metallic elements. Addition of ethylene glycol generated polymerization in a 1:2:4 ratio (nitrate precursors, citric acid chelating agent, and ethylene glycol, respectively). Two-step thermal decomposition (200 °C and 600 °C) led to the generation of nanosized crystalline phases. Such powders were ground in a ball mill and later sintered at 1350 °C for 10 h to produce the desired crystalline phase (ICDD 00-035-1112 for $Fe_{0.7}Cr_{1.3}O_3$).

Both $Fe_{0.7}Cr_{1.3}O_3$ and LSM were mixed with 8YSZ (Tosoh) in a 1:1 vol. ratio to avoid delamination with the electrolyte and to obtain a mixed ionic–electronic material, respectively. Electronic conductivity is offered by LSM (and selective O_2 activation), while ionic conductivity is provided by 8YSZ. Then, these mixtures were ball milled, mixed with an organic binder, and passed through a triple roll mill to produce inks for screen printing.

2.2. Fabrication of the Sensor Device

A four-working-electrode (WE) multidevice was constructed to measure up to four different WE compositions simultaneously, as shown in Figure 1. The electrolyte acts as a support, and it consists of a dense 50 mm diameter disk made of 8YSZ (Tosoh). The disk was uniaxially pressed and then calcined in two steps: (1) 1000 °C for 4 h to machine holes for later wiring and (2) 1450 °C for 10 h to densify the electrolyte

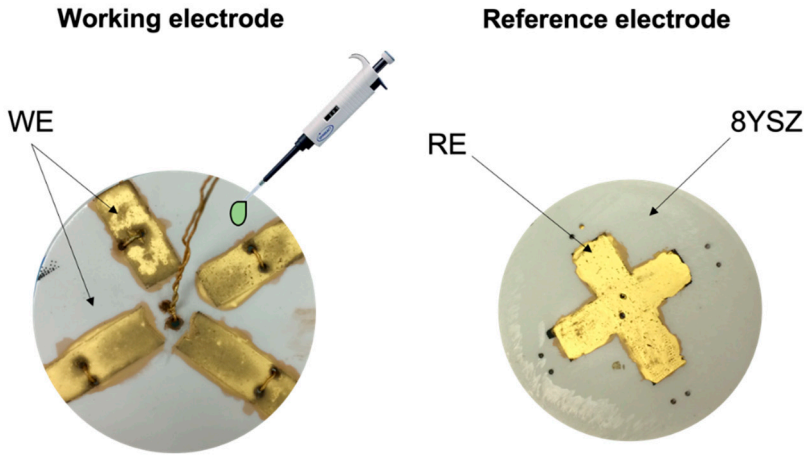

Figure 1. Scheme of the device that consists of a dense 8YSZ electrolyte with a common LSM/8YSZ reference electrode (**right**). Each of the working electrodes ($Fe_{0.7}Cr_{1.3}O_3$) is infiltrated using a micropipette with several elements (**left**). The lead wires are mechanically fixed to the device using 5 boreholes.

Electrodes were screen printed in a rectangular shape: four $Fe_{0.7}Cr_{1.3}O_3$/8YSZ electrodes on one side of the electrolyte and only one LSM/8SZ on the other side. This configuration is convenient because it consists of a reference electrode for oxygen, which is common, and four different working electrodes for testing different catalytic materials to functionalize the electrode by nanoparticle infiltration. Replacing Pt, which is usually employed as RE [12,13,51–57], with LSM/8SZ results in a larger triple-phase boundary (TPB). This means an increment in the contact point between electronic and ionic materials and the gas. A screen-printed gold layer was used as the current collector (900 °C for 2 h) on top of the electrodes, while silver paste was employed to assure the attachment of the lead wires to the electrodes.

The working electrode is infiltrated with several nanocatalysts: Ti, Al, Nb, Ba, and Pd. Nitrate precursor solutions of the aforementioned elements were dropped onto the WE. The solution filled the pores through the capillarity, ensuring full coverage of the electrode surface. The device was then exposed to a thermal treatment to eliminate the organic fraction. First, it was treated with argon at 550 °C for 4 h. Subsequently, the gas composition was changed to 5% H_2 in Ar, and the device was exposed again at 550 °C for another 4 h. The stability of the LSM electrode was confirmed after thermal treatment in these gas atmospheres. After testing each of the aforementioned elements, a second Ni infiltration was performed for each, following the same procedure described previously. Nickel has already been reported to increase device selectivity to C_2H_4 [41].

3. Sample Characterization

The obtained crystalline phases were identified through X-ray diffraction analysis (XRD) using a PANalytical Cubix fast diffractometer (CuKα1 radiation (λ = 1.5406 Å) and an X′Celerator detector in Bragg–Brentano configuration). X′Pert Highscore Plus was employed to analyze the patterns measured in the 2θ range from 10° to 90°. The cross-sections of the devices were studied by SEM and energy-dispersive X-ray spectroscopy (EDS) using a ZEISS Ultra55 field-emission scanning electron microscope.

Regarding electrochemical characterization, the voltage was measured (Keithley 3706) as the potential difference generated between both electrodes (no current applied) at 550 °C and different C_2H_4 and CO concentrations. The flow of gases was controlled by means of mass flow controllers, and the total gas flow was set to 550 mL/min (with 6% O_2 and balanced with argon). The sensor response (V_{cell}, mV) was corrected, taking into consideration the background gas consisting of 6% O_2/Ar, and it was defined as:

$$V_{cell} = V_{analyte} - V_{background}$$

When the sample was stabilized at 550 °C, either C_2H_4 or CO concentration pulses were performed from 50 ppm (used as base gas) to 100, 150, and 200 ppm. In order to determine the cross-sensitivity, this procedure was repeated at a fixed concentration of 200 ppm opposing gas. Finally, impedance sweeps from 0.03 Hz to 1 MHz were measured (Autolab PGSTAT204 with an FRA32M module) for both C_2H_4 and CO at 200 ppm.

4. Results and Discussion

4.1. Microstructural Characterization

XRD patterns of $Fe_{0.7}Cr_{1.3}O_3$ and LSM (Figure S1) confirm that the phases for both materials were formed as desired, i.e., no diffraction peaks were detected for other phases or the precursor. Postmortem SEM characterization of the device was carried out to determine the dispersion of the nanoparticles over the electrode grains. In every pore, the distribution of $Fe_{0.7}Cr_{1.3}O_3$ and 8YSZ grains is homogeneous, although the grain size is different, i.e., $Fe_{0.7}Cr_{1.3}O_3$ grains are larger (Figure 2). Layer thickness observed for the WE and RE is 34 and 13 μm, respectively.

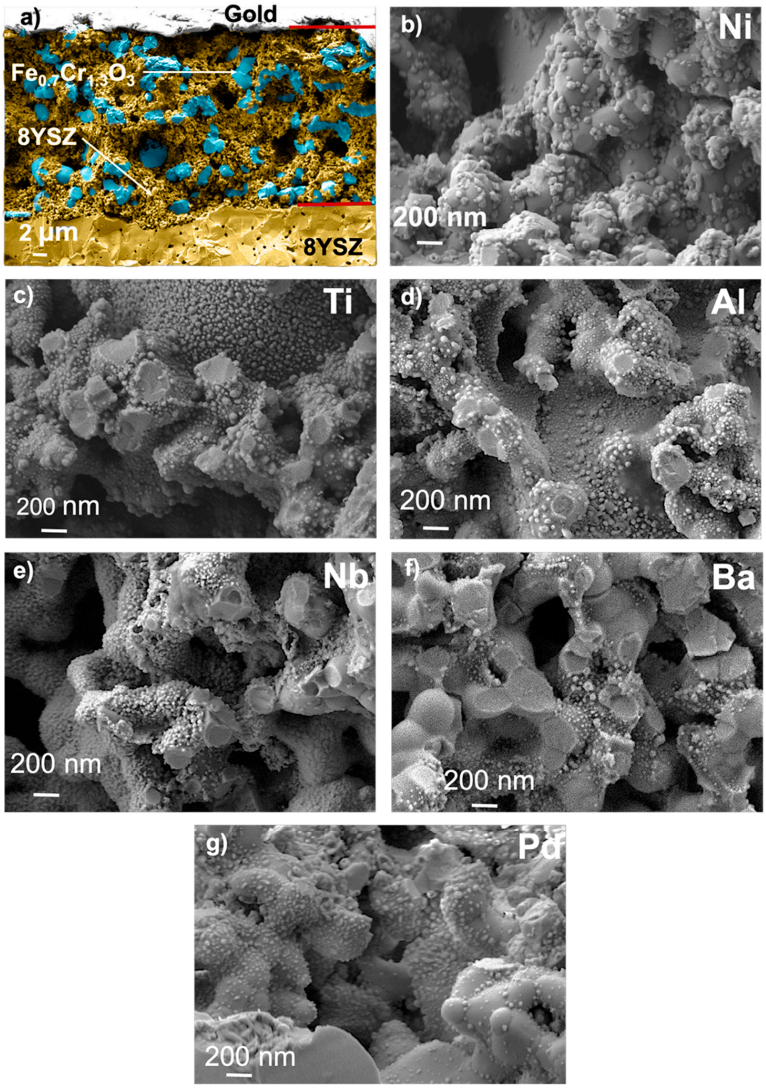

Figure 2. FESEM images of the working electrode cross-section for the bare sensor with 8YSZ in yellow and $Fe_{0.7}Cr_{1.3}O_3$ in blue (**a**) and several infiltrations: (**b**) Ni, (**c**) Ti, (**d**) Al, (**e**) Nb, (**f**), Ba and (**g**) Pd. Nanoparticles for each element can be observed. Additionally, different sizes of nanoparticles can be observed when nickel is added to the first element infiltrated. $Fe_{0.7}Cr_{1.3}O_3$ and 8YSZ grains are observed to be homogeneously distributed.

A deeper look at the working electrode shows a good distribution of the nanoparticles all over the electrode for all the performed infiltrations (Figure 2). Oxide nanoparticles are equally attached to both $Fe_{0.7}Cr_{1.3}O_3$ and 8YSZ grains, and therefore, the surface active area for electrochemical sensing is enlarged. Two nanoparticle size ranges can be observed for each infiltration. Nanoparticles formed upon infiltration of Ti, Nb, Al, Ba, and Pd are smaller than Ni-based nanoparticles. Energy-dispersive X-ray spectroscopy (EDX) analysis and subsequent comparison with a device infiltrated with only nickel confirm that the largest nanoparticles are made of nickel [41]. Thus, the smaller nanoparticles must be the second element infiltrated into the electrode (EDX was limited and could not identify the main element of these small nanoparticles due to the limits of this technique). The nanoparticles are well distributed and constant along the electrode, except at a lower extent for Ba and Pd. Moreover, no presence of nanoparticles is observed in the reference electrode, confirming that the infiltration was selectively carried out in the WE. Thus, any improvement in sensor performance in comparison to the bare sensor can be attributed to the infiltration in the working electrode. The poor distribution of Ba and Pd may cause low activity of these electrodes to C_2H_4 when compared to other elements such as Ti or Al.

4.2. Electrochemical Characterization

In an exhaust-gas-like atmosphere, where several pollutants such as hydrocarbons, CO, NO_x, O_2, etc., can be present, several oxidation and reduction reactions can take place on both the WE and RE. The kinetics of one of these reactions will prevail on each electrode, controlling the electrode, and the difference in voltage between both electrodes will provide the final device response. Ideally, the oxidation of the reducing agent will take place in the WE when achieving the equilibrium (Equation (1) or (2)), while O_2 is reduced in the RE (Equation (3)). The electrode must be porous to facilitate the diffusion of the gaseous analyte to the contact points with both electronic and ionic conductors (TPB).

Both anodic and cathodic reactions are coupled by the oxygen ion diffusion through the 8YSZ electrolyte. This kind of sensor follows the so-called theory of mixed potential, and therefore, the response of the device is kinetically controlled [13,35,58–60]. A zero current is imposed, and a mixed potential is established in each electrode (Equation (1) or (2) for the anodic reaction and Equation (3) for the cathodic reaction) when the steady state is reached. The final voltage of the cell is given by this built-up mixed-potential difference.

Additionally, a heterogeneous catalytic conversion process could take place at the electrodes. The analytes could react with locally adsorbed O_2 (Equations (4)–(6)), the electrochemical reaction not being favored [14,61–63]. The reaction network on the electrodes can be described by the following reactions.

$$CO + O^{2-} \rightarrow CO_2 + 2e^- \quad (1)$$

$$C_2H_4 + 6O^{2-} \rightarrow 2CO_2 + 2H_2O + 12e^- \quad (2)$$

$$\frac{1}{2}O_2 + 2e^- \rightarrow O^{2-} \quad (3)$$

$$CO + \frac{1}{2}O_2 \rightarrow CO_2 \quad (4)$$

$$C_2H_4 + 3O_2 \rightarrow 2CO + 2H_2O \quad (5)$$

$$C_2H_4 + \frac{1}{2}O_2 \rightarrow CH_3COH \quad (6)$$

4.2.1. Potentiometric Characterization

As previously reported, the (catalytically nonactivated) bare sensor response is not specific to C_2H_4 [41]. The device is exposed to concentration pulses of both pure CO and C_2H_4 from 50 to 200 ppm for 20 min. Additionally, the device response is measured for the same concentration pulses of one analyte but with a fixed concentration of 200 ppm of the other, as shown in Figure 3. This counter plot helps to summarize the sensor response to

both C_2H_4 and CO. In these plots, the *x*- and *y*-directions are CO and C_2H_4 concentrations, respectively. The colormap indicates the voltage response offered by the sensor when exposed to a given concentration of analytes. Thus, a device selective to C_2H_4 must show an increase within the *y*-direction, with its response in the *x*-direction remaining constant. Figures 3 and 4 display how the response to both C_2H_4 and CO is similar, and therefore, the C_2H_4 electrochemical reaction is not favored. As observed in Figure 3, the lines of constant potential are diagonal, increasing from left to right. This confirms the lack of selectivity to C_2H_4. Figure 4 shows the transient response for different scenarios with C_2H_4 and CO, confirming similar responses. This indicates a high cross-sensitivity toward CO, and therefore, the device is unable to measure C_2H_4 in an exhaust-gas-like atmosphere.

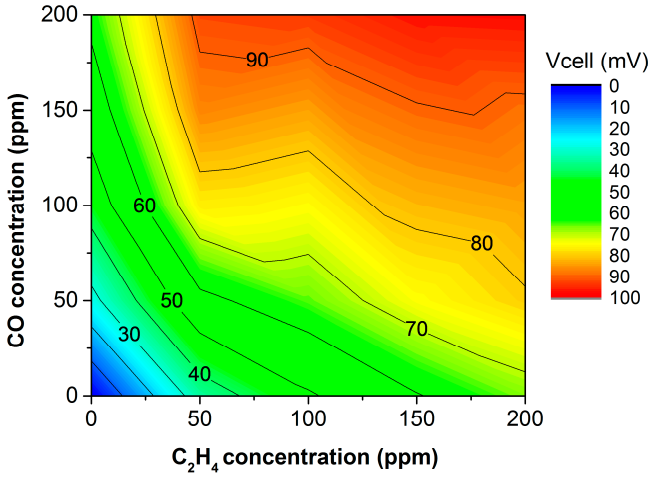

Figure 3. Sensor response (V_{cell}) to analyte concentration prior to any infiltration. The device could not detect C_2H_4 due to cross-sensitivity toward CO. Standard error ± 0.02 mV.

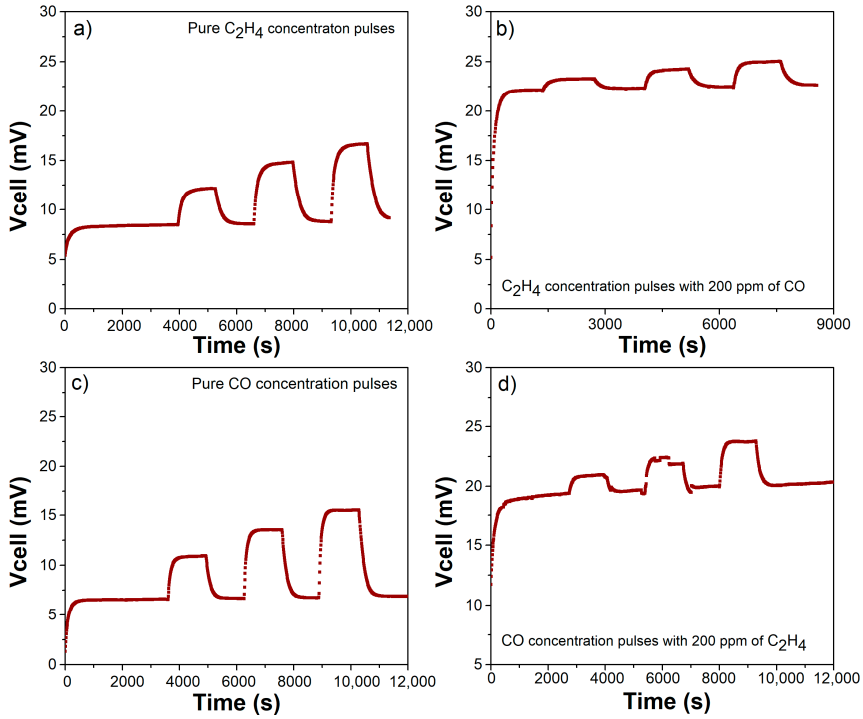

Figure 4. Bare sensor transient response prior to any infiltration to improve catalytic activity: (**a**) pure C_2H_4, (**b**) C_2H_4 with 200 ppm of CO as background, (**c**) pure CO, and (**d**) CO with 200 ppm of C_2H_4 as background.

Therefore, the working electrode should be catalytically activated to promote the electrochemical reaction of C_2H_4. Several catalyst nanoparticles are infiltrated into each channel to achieve this promotion of the C_2H_4 reaction rate. As several channels are measured, the response is normalized to enable comparison. After the infiltration of nanoparticles in dry conditions, it was found that Ti and Al led to an increase in the electrochemical reaction of C_2H_4 (Figure 5). Thus, this reaction is kinetically favored. It should be noted that the response to C_2H_4 is not affected by the addition of 200 ppm of CO. Thus, the device is able to detect C_2H_4 even in the presence of CO. On the other hand, Nb, Ba, and Pd infiltration provide a poorer response in dry conditions. Despite improving the response in comparison to the bare sensor, the cross-sensitivity toward CO is too high, albeit for C_2H_4 detection purposes (Figure 5).

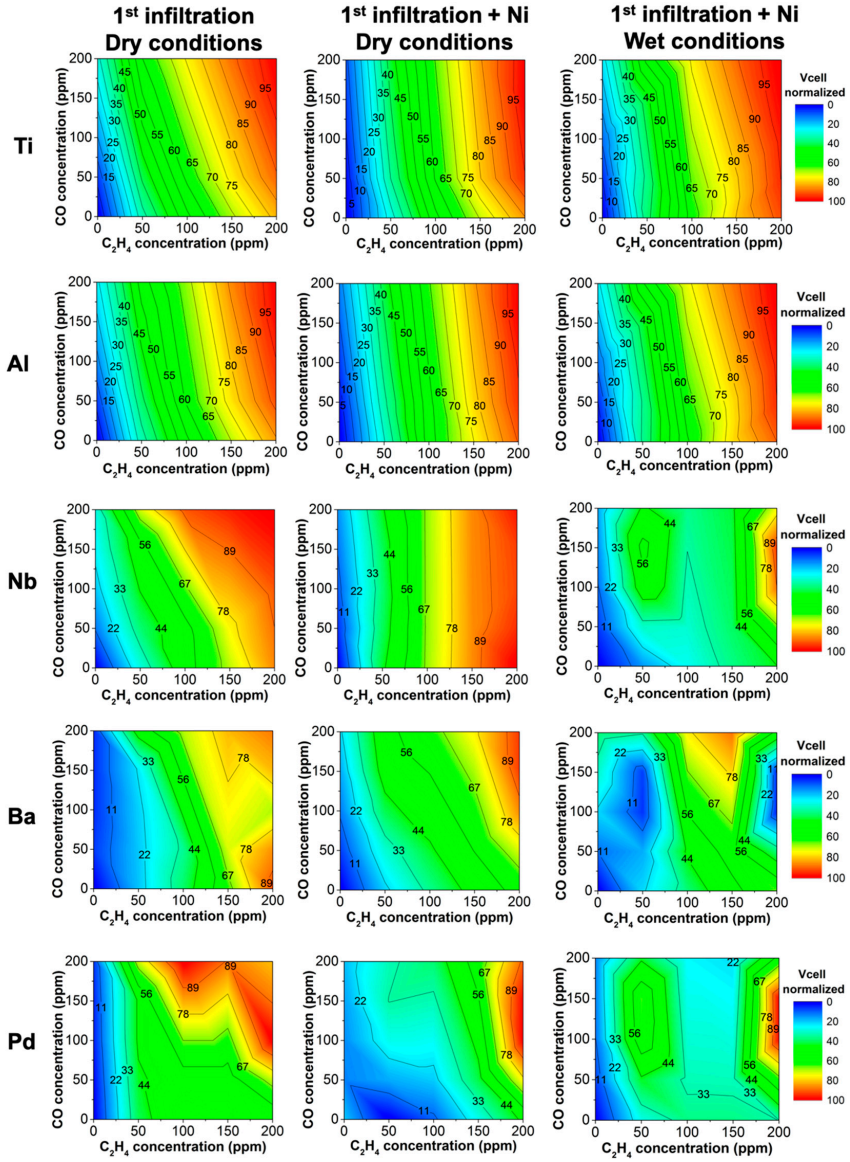

Figure 5. Device performance as a function of C_2H_4 and CO concentration after infiltration of the WE. The first column shows the sensor response for the first element infiltrated in dry conditions, the second column depicts the sensor response after an additional infiltration with Ni in dry conditions, and the last column shows the response after the second infiltration with Ni in wet conditions. Each row indicates the first element infiltrated. Standard errors of sensor response for each infiltrated element are: ±0.02 mV for Ti, ±0.03 mV for Al, ±0.07 mV for Nb, ±0.07 mV for Nb, ±0.003 mV for Ba, and 0.01 mV for Pd.

The subsequent infiltration with Ni enhanced the sensor detection of C_2H_4 even more for Ti and Al devices (Figure 5). Additionally, this second infiltration improved the performance of the Nb-infiltrated device: the C_2H_4 electrochemical reaction is promoted, providing a response dependent on C_2H_4 but not on CO (Figure 5). Unfortunately, cross-sensitivity toward CO of Ba and Pd devices is not improved adequately for sensing purposes (Figure 5), as previously attributed to the poor dispersion of Ba and Pd in the electrode (Figure 2).

Ti and Al devices are still selective to C_2H_4 even when the device is exposed to a wet gas stream (3% vol. H_2O). As previously reported, H_2O usually negatively affects the sensor response, i.e., increasing the cross-sensitivity toward CO [32,64–66]. However, the catalytically activated sensor is still selective to C_2H_4 under humid atmospheres. The low cross-sensitivity toward CO and H_2O makes this configuration promising for hydrocarbon detection in atmospheres with several pollutants. The improvement in sensing capability might be due to the improved electrocatalytic properties of the material itself. Nonetheless, in the case of Nb, the addition of water affects the device performance, and thus, the device is no longer selective to C_2H_4.

4.2.2. Electrochemical Impedance Spectroscopy Analysis

Electrochemical impedance spectroscopy was performed for each one the five infiltrated elements, exposing the device to 200 ppm of pure CO and C_2H_4. The EIS measurement procedure is as follows: first the bare sensor, then with the addition of the first element, and finally for the first element plus Ni in dry and wet conditions.

Figure 6 displays Nyquist plots from 0.03 Hz to 1 MHz. The sensors infiltrated with Ti, Al, Ba, and Pd present two-arc contributions. The respective Bode plots are depicted in Figure S2. The equivalent circuit proposed consists of two parallel combinations of resistance-constant phase elements (R-CPE) connected in series. However, the Nb-infiltrated sensor has a three-arc contribution that was fitted to an equivalent circuit consisting of three parallel combinations of R-CPE. This study is focused on Ti, Al, and Nb, as they exhibited the best sensing properties. The arc shape at high frequencies in the Nyquist plot is similar in all cases, and this indicates the similar behavior of oxide ion transport through crystalline grain, as expected from the identical electrolyte and electrode backbone structure.

In general terms, the first arc contribution (appearing at higher frequencies and with $C = 10^5$–10^6 F as in Figure 6 and Figure S3) at 550 °C may be due to the electrode–8YSZ electrolyte interface [67–69]. When the device is exposed to C_2H_4 and CO, this resistance remains almost constant for the bare sensors, as well as when the device is infiltrated, firstly with Ti, Al, and Nb and secondly with Ni (see Figure 6). Accordingly, the ionic mobility remains almost unaffected, i.e., ion diffusion in the bulk is not affected by the addition of the nanocatalysts.

The second arc contribution appearing at lower frequencies (10^3–10^4 F, as depicted in Figure 6) is related to electrocatalytic processes taking place at the surface of the electrode and depending on the type of infiltration performed. The effect of this lower-frequency contribution can also be observed in the Bode plots in the range from 0.03 to 145 Hz (Figure S2). In the case of the bare sensor, the polarization resistance is almost the same for both C_2H_4 and CO, as shown for example in Figure 6. This agrees with the potentiometric characterization (Figure 5) and can explain the lack of selectivity to C_2H_4.

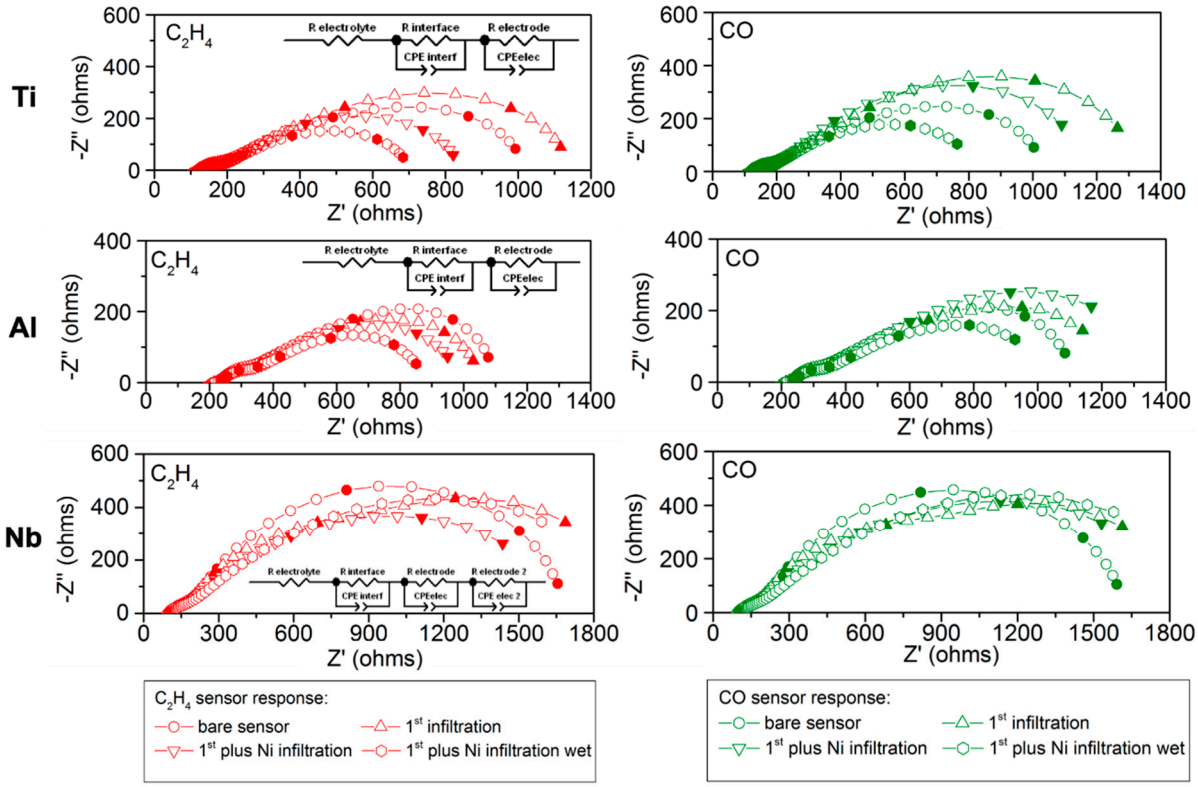

Figure 6. EIS results for the devices infiltrated with Ti, Al, and Nb for the bare sensor (dots), first infiltration (triangle), additional infiltration with Ni in dry conditions (inverse triangle), and additional infiltration with nickel in wet conditions (hexagon). C_2H_4 response is depicted in red on the left side, and CO response is shown in green on the right side. Inset indicates the equivalent circuit fitting the response: two resistance-constant phase-parallel elements for Ti and Al, while for Nb, there is an additional resistance-constant phase-parallel element.

For both Al and Ti, their infiltration led to an increase in the CO contribution, while the C_2H_4 contribution decreased (as observed in Figures 6 and 7). This agrees with the potentiometric study and can explain the better performance. Electrochemical reaction to C_2H_4 is catalytically promoted. The second infiltration with nickel decreases both contributions, although the decrease for C_2H_4 is higher. Therefore, the C_2H_4 resistance is lesser than CO, as observed in Figure 7, and this explains again the better performance of the device for both configurations in dry conditions. This is also backed by the evolution of the low-frequency contribution observed in the Bode plots in Figure S2.

As aforementioned, H_2O can have a negative influence on the sensor performance affecting the output voltage and cross-sensitivity. Therefore, it is sensible to the effect of H_2O on the sensor response. The addition of 3% H_2O to the gas flow causes a further decrease in both contributions. However, the C_2H_4 contribution is smaller than that of CO. This agrees with the performed potentiometric study, and it confirms that the C_2H_4 reaction is more favored.

Thus, according to the potentiometric study and the electrochemical impedance, both Ti and Al plus Ni are strong candidates for C_2H_4 detection, as they promote the electrochemical reaction of C_2H_4 and even partial heterogeneous catalysis of CO.

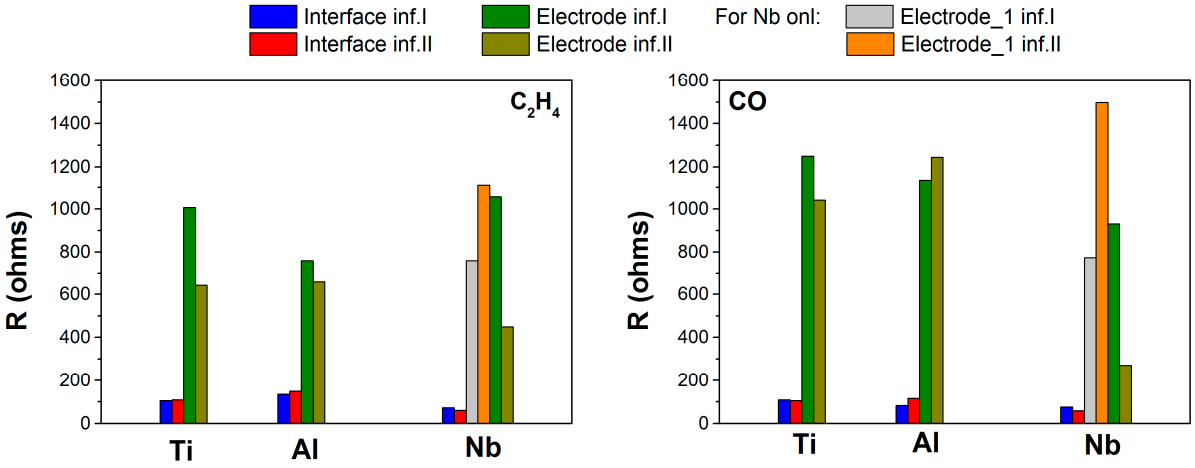

Figure 7. Fitting results for the first infiltration with each element (blue and green) and second infiltration with Ni (red and brown). Resistances related to interface and electrode processes are calculated. On the left side, C_2H_4 response is depicted, while on the right side, the response to CO is depicted. In the case of Nb, an additional electrode contribution appears (gray and yellow). The maximum chi-square values obtained in the fitting of each element are: 1.5×10^{-4} for Ti, 1.7×10^{-4} for Al, and 4.59×10^{-6} for Nb.

On the other hand, Nb infiltration behaves differently. According to the potentiometric study, the device has a strong cross-sensitivity toward CO (see Figures 6 and 7). The behavior shows a first contribution similar for both analytes and a second that is smaller for CO. Conversely, the addition of Ni reversed this behavior, i.e., the first contribution is increased for both analytes, but the increment is much higher for CO. In the case of the second contribution, it is reduced for both analytes. Although the reduction of the second electrode element is higher for CO, the first electrode contribution has the greatest influence. This causes the C_2H_4 total electrode contribution for Nb plus Ni infiltration to be lesser than that of CO, and therefore, its electrochemical reaction is promoted, as observed in the potentiometric analysis in Figure 5. The addition of 3 vol. % H_2O provides a similar contribution for both analytes, and therefore, this explains the lack of selectivity to C_2H_4 in the potentiometric study, both analytes are promoted equally under humid atmospheres.

On the other hand, Ba and Pd offer a similar response when infiltrated, even when a second infiltration with Ni is carried out in dry and wet conditions, as can be observed in Figure S3. The potentiometric study already stated that the C_2H_4 reaction was not promoted, and therefore, the cross-sensitivity toward CO is not ameliorated.

5. Conclusions

The catalytic functionalization of a potentiometric sensor enabled enhancing selectivity toward C_2H_4 while keeping low cross-sensitivity toward CO and H_2O. The sensor is composed of $Fe_{0.7}Cr_{1.3}O_3$/8YSZ and LSM/8YSZ as working and reference electrodes, respectively, and 8YSZ as solid-state electrolyte.

Potentiometric characterization showed that electrode surface decoration with Ti or Al resulted in improved sensor performance. The device is selective toward C_2H_4, with low cross-sensitivity toward CO. Moreover, a second infiltration with Ni to (i) largely improved sensor performance in dry conditions and (ii) provided a device able to selectively measure C_2H_4 in moist conditions. The nanocatalysts promoted the selective C_2H_4 electrochemical oxidation even in the presence of CO. Consequently, these materials are potential candidates for C_2H_4 detection.

On the other hand, infiltration with Nb, Pd, and Ba, despite improving the bare sensor signal, failed to provide an adequate sensor response for the purpose of hydrocarbon sensing. However, a Nb-infiltrated device after a second infiltration with Ni ameliorated its performance in dry conditions, although in moist conditions, the performance is worse.

Electrochemical impedance spectroscopy analysis revealed that the resistance of the electrode–electrolyte interface (C = 10^5–10^6 F) was unaffected practically by the catalyst infiltrations. Conversely, low-frequency resistances associated with catalytic processes occurring on the electrode surface varied upon catalyst infiltration. For Ti and Al infiltrations, either having a second Ni infiltration or not, the polarization resistance to CO was higher than C_2H_4. Thus, the better performance of C_2H_4 with low cross-sensitivity toward CO may be explained by such a difference. Incorporation of nanoparticles onto the working electrode was confirmed by means of FESEM analysis, revealing that Ti and Al are homogeneously distributed.

Accordingly, the sequential infiltration with bifunctional nanocatalysts enabled modifying the kinetics of electrode surface catalytic reactions, as inferred from impedance spectroscopy analysis at low frequencies. This surface functionalization enabled boosting the electrochemical oxidation of C_2H_4, and this process became the main contributor to the working electrode response. Specifically, the reported sensor configurations comprising Ti or Al plus Ni nanoparticles are suitable for applications in conditions similar to those of exhaust gases from combustion or other thermochemical processes.

Supplementary Materials: The following are available online at https://www.mdpi.com/article/10.3390/chemosensors9100274/s1, Figure S1: X-ray diffraction pattern of both LSM and $Fe_{0.7}Cr_{1.3}O_3$ powders at room temperature; Figure S2: Bode plots for devices infiltrated with Ti, Al, and Nb for the bare sensor (dots), first infiltration (triangle), additional infiltration with Ni in dry conditions (inverse triangle), and additional infiltration with nickel in wet conditions (hexagon). C_2H_4 response is depicted in red on the left side, and CO response is shown in green on the right side. The Bode plots correspond to the Nyquist plots depicted in Figure 6; Figure S3: EIS results for the devices infiltrated with Ba and Pd for the bare sensor (dots), first infiltration (triangle), additional infiltration with nickel in dry conditions (inverse triangle), and additional infiltration with nickel in wet conditions (hexagon). C2H4 response is depicted in red on the left side, and CO response is shown in green on the right side.

Author Contributions: Conceptualization, J.M.S. and F.T.-R.; Methodology, F.T.-R.; Investigation, J.M.S. and F.T.-R.; Resources, J.M.S.; Data Curation, F.T.-R.; Writing-Original Draft Preparation, J.M.S. and F.T.-R.; Writing-Review & Editing, J.M.S. and F.T.-R.; Supervision, J.M.S.; Funding Acquisition, J.M.S. All authors have read and agreed to the published version of the manuscript.

Funding: Funding from the Spanish Government (Grants FPU13/03478, AP-2003-03478, and RTI2018-102161) is kindly acknowledged.

Institutional Review Board Statement: Not applicable.

Informed Consent Statement: Not applicable.

Data Availability Statement: Not applicable.

Conflicts of Interest: The authors declare no conflict of interest.

References

1. Schraufnagel, D.E.; Balmes, J.R.; Cowl, C.T.; de Matteis, S.; Jung, S.H.; Mortimer, K.; Perez-Padilla, R.; Rice, M.B.; Riojas-Rodriguez, H.; Sood, A.; et al. Air pollution and noncommunicable diseases: A review by the Forum of International Respiratory Societies' Environmental Committee, part 2: Air pollution and organ systems. *Chest* **2019**, *155*, 417–426. [CrossRef]
2. Schraufnagel, D.E.; Balmes, J.R.; Cowl, C.T.; de Matteis, S.; Jung, S.-H.; Mortimer, K.; Perez-Padilla, R.; Rice, M.B.; Riojas-Rodriguez, H.; Sood, A.; et al. Air pollution and noncommunicable diseases. *Chest* **2019**, *155*, 409–416. [CrossRef]
3. Krzyzanowski, M.; Kuna-Dibbert, B.; Schneider, J. (Eds.) *Health Effects of Transport-Related Air Pollution*; World Health Organization (WHO): Copenhagen, Denmark, 2005.
4. Horizon Europe. Work Programme 2021–2022: Climate, Energy and Mobility. Call: HORIZON-CL5-2021-D5-01. Available online: https://ec.europa.eu/info/funding-tenders/opportunities/docs/2021-2027/horizon/wp-call/2021-2022/wp-8-climate-energy-and-mobility_horizon-2021-2022_en.pdf (accessed on 15 September 2021).
5. Fu, S.; Gu, Y. Highway toll and air pollution: Evidence from Chinese cities. *J. Environ. Econ. Manag.* **2017**, *83*, 32–49. [CrossRef]
6. Corvec, S.S.-L.; Mercier, A.; Ovtracht, N.; Chevallier, A. Urban toll and electric vehicles: The winning ticket for Lyon Metropolitan Area (France). *Res. Transp. Econ.* **2019**, *73*, 17–33. [CrossRef]

7. Croci, E. Urban road pricing: A comparative study on the experiences of London, Stockholm and Milan. *Transp. Res. Procedia* **2016**, *14*, 253–262. [CrossRef]
8. H2020 Work Programme 2018–2020: Smart, Green and Integrated Transport. Call: H2020-MG-2018-2019-2020. Available online: https://ec.europa.eu/info/funding-tenders/opportunities/portal/screen/opportunities/topic-details/lc-mg-1-1-2018 (accessed on 25 April 2019).
9. H2020 Work Programme 2018–2020: Smart, Green and Integrated Transport. Call: H2020-MG-2018-2019-2020. Available online: https://ec.europa.eu/info/funding-tenders/opportunities/portal/screen/opportunities/topic-details/lc-mg-1-9-2019 (accessed on 25 April 2019).
10. Yu, J.; Deng, S.; Jin, H.; Huang, M.; Wang, S.; Zhang, X. Gas phase reaction combined light-regulated electrochemical sensing technique for improved response selectivity and sensitivity to hydrocarbons. *Ionics* **2020**, *26*, 6351–6357. [CrossRef]
11. Ikeda, H.; Iio, A.; Anggraini, S.A.; Miura, N. Impedancemetric YSZ-based oxygen sensor using $BaFeO_3$ sensing-electrode. *Sens. Actuators B Chem.* **2016**, *243*, 279–282. [CrossRef]
12. Macam, E.R.; White, B.M.; Blackburn, B.M.; di Bartolomeo, E.; Traversa, E.; Wachsman, E.D. La_2CuO_4 sensing electrode configuration influence on sensitivity and selectivity for a multifunctional potentiometric gas sensor. *Sens. Actuators B Chem.* **2011**, *160*, 957–963. [CrossRef]
13. Miura, N.; Sato, T.; Anggraini, S.A.; Ikeda, H.; Zhuiykov, S. A review of mixed-potential type zirconia-based gas sensors. *Ionics* **2014**, *20*, 901–925. [CrossRef]
14. Striker, T.; Ramaswamy, V.; Armstrong, E.N.; Willson, P.D.; Wachsman, E.D.; Ruud, J.A. Effect of nanocomposite Au–YSZ electrodes on potentiometric sensor response to NOx and CO. *Sens. Actuators B Chem.* **2013**, *181*, 312–318. [CrossRef]
15. Ueda, T.; Abe, H.; Kamada, K.; Bishop, S.R.; Tuller, H.L.; Hyodo, T.; Shimizu, Y. Enhanced sensing response of solid-electrolyte gas sensors to toluene: Role of composite Au/metal oxide sensing electrode. *Sens. Actuators B Chem.* **2017**, *252*, 268–276. [CrossRef]
16. Guth, U.; Wiemhöfer, H.-D. Gas sensors based on oxygen ion conducting metal oxides. In *Gas Sensors Based on Conducting Metal Oxides*; Elsevier: Amsterdam, The Netherlands, 2018; pp. 13–60. [CrossRef]
17. Zeng, J.; Xu, Y.; Yu, J.; Zhang, X.; Zhang, X.; Jin, H.; Jin, Q.; Shen, W.; Zou, J.; Deng, S.; et al. Compact yttria-stabilized zirconia based total NO_x sensor with a dual functional Co_3O_4/NiO sensing electrode. *ACS Sens.* **2019**, *4*, 2150–2155. [CrossRef]
18. Iio, A.; Ikeda, H.; Anggraini, S.A.; Miura, N. Potentiometric YSZ-Based Oxygen Sensor Using BaFeO3 Sensing-Electrode. *Electrochem. Commun.* **2014**, *48*, 134–137. [CrossRef]
19. Anggraini, S.A.; Fujio, Y.; Ikeda, H.; Miura, N. YSZ-based sensor using Cr-Fe-based spinel-oxide electrodes for selective detection of CO. *Anal. Chim. Acta* **2017**, *982*, 176–184. [CrossRef]
20. Zou, J.; Zheng, Y.; Li, J.; Zhan, Z.; Jian, J. Potentiometric NO_2 sensors based on thin stabilized zirconia electrolytes and asymmetric (La0. 8Sr0. 2) 0.95 MnO_3 electrodes. *Sensors* **2015**, *15*, 17558–17571. [CrossRef]
21. Dietrich, S.; Kusnezoff, M.; Michaelis, A. Studies of indium tin oxide-based sensing electrodes in potentiometric zirconia solid electrolyte gas sensors. *Sensors* **2021**, *21*, 2345. [CrossRef]
22. Chevallier, L.; Traversa, E.; di Bartolomeo, E. Propene detection at high temperatures using highly sensitive non-nernstian electrochemical sensors based on Nb and Ta oxides. *J. Electrochem. Soc.* **2010**, *157*, J386–D581. [CrossRef]
23. Sekhar, P.K.; Moore, Z.; Aravamudhan, S.; Khosla, A. A new low-temperature electrochemical hydrocarbon and NO_x sensor. *Sensors* **2017**, *17*, 2759. [CrossRef]
24. Fujio, Y.; Plashnitsa, V.V.; Elumalai, P.; Miura, N. Stabilization of sensing performance for mixed-potential-type zirconia-based hydrocarbon sensor. *Talanta* **2011**, *85*, 575–581. [CrossRef]
25. Jin, H.; Plashnitsa, V.V.; Breedon, M.; Miura, N. Compact YSZ-rod-based hydrocarbon sensor utilizing metal-oxide sensing-electrode and Mn-based reference-electrode combination. *Electrochem. Solid-State Lett.* **2011**, *14*, J23–J25. [CrossRef]
26. Sekhar, P.K.; Ludwig, T.; Wilhelm, M.; Graf, D.; Riheen, M.A.; Mathur, S. Potentiometric ethene sensor for postharvest detection applications. *J. Electrochem. Soc.* **2019**, *166*, B1477–B1482. [CrossRef]
27. Saberi, M.; Mortazavi, Y.; Khodadadi, A. Dual selective Pt/SnO_2 sensor to CO and propane in exhaust gases of gasoline engines using Pt/$LaFeO_3$ filter. *Sens. Actuators B Chem.* **2015**, *206*, 617–623. [CrossRef]
28. Plashnitsa, V.V.; Anggraini, S.A.; Miura, N. CO sensing characteristics of YSZ-based planar sensor using Rh-sensing electrode composed of tetrahedral sub-micron particles. *Electrochem. Commun.* **2011**, *13*, 444–446. [CrossRef]
29. Yang, B.; Wang, C.; Xiao, R.; Yu, H.; Wang, J.; Xu, J.; Liu, H.; Xia, F.; Xiao, J. CO response characteristics of $NiFe_2O_4$ sensing material at elevated temperature. *J. Electrochem. Soc.* **2019**, *166*, B956–B960. [CrossRef]
30. Yang, B.; Wang, C.; Xiao, R.; Yu, H.; Huang, C.; Wang, J.; Xu, J.; Liu, H.; Xia, F.; Xiao, J. High NH_3 selectivity of $NiFe_2O_4$ sensing electrode for potentiometric sensor at elevated temperature. *Anal. Chim. Acta* **2019**, *1089*, 165–173. [CrossRef]
31. Schönauer-Kamin, D.; Fleischer, M.; Moos, R. Influence of the V_2O_5 content of the catalyst layer of a non-Nernstian NH_3 sensor. *Solid State Ion.* **2014**, *262*, 270–273. [CrossRef]
32. Toldra-Reig, F.; Serra, J.M. Development of potentiometric sensors for C_2H_4 detection. *Sensors* **2018**, *18*, 2992. [CrossRef]
33. Bhardwaj, A.; Kumar, A.; Sim, U.; Im, H.-N.; Song, S.-J. Synergistic enhancement in the sensing performance of a mixed-potential NH_3 sensor using SnO_2@ $CuFe_2O_4$ sensing electrode. *Sens. Actuators B Chem.* **2020**, *308*, 127748. [CrossRef]
34. Fergus, J.W. Solid electrolyte based sensors for the measurement of CO and hydrocarbon gases. *Sens. Actuators B Chem.* **2007**, *122*, 683–693. [CrossRef]

35. Di Bartolomeo, E.; Grilli, M.L.; Traversa, E.; Dutta, A.; Ishihara, T.; Nishiguchi, H.; Takita, Y. Sensing mechanism of potentiometric gas sensors based on stabilized zirconia with oxide electrodes. *J. Electrochem. Soc.* **2004**, *151*, H133–H127. [CrossRef]
36. Chevallier, L.; di Bartolomeo, E.; Grilli, M.L.; Traversa, E. High temperature detection of CO/HCs gases by non-Nernstian planar sensors using Nb_2O_5 electrode. *Sens. Actuators B Chem.* **2008**, *130*, 514–519. [CrossRef]
37. McCulloch, M.T.; Langford, N.; Duxbury, G. Real-time trace-level detection of carbon dioxide and ethylene in car exhaust gases. *Appl. Opt.* **2005**, *44*, 2887–2894. [CrossRef] [PubMed]
38. Grosjean, E.; Rasmussen, R.A.; Grosjean, D. Ambient levels of gas phase pollutants in Porto Alegre, Brazil. *Atmos. Environ.* **1998**, *32*, 3371–3379. [CrossRef]
39. Poulopoulos, S.; Samaras, D.; Philippopoulos, C. Regulated and unregulated emissions from an internal combustion engine operating on ethanol-containing fuels. *Atmos. Environ.* **2001**, *35*, 4399–4406. [CrossRef]
40. Storey, J.M.; Lewis, S.A., Sr.; West, B.H.; Shean, P.H.; Scott Sluder, C.; Wagner, R.M.; Domingo, N.; Thomas, J.; Kass, M. *Hydrocarbon Species in the Exhaust of Diesel Engines Equipped with Advanced Emissions Control Devices*; Final Report CRC Project No. AVFL-10b-2; Fuels, Engines, and Emissions Research Center, Oak Ridge National Laboratory: Oak Ridge, TN, USA, 2005.
41. Toldra-Reig, F.; Serra, J.M. Surface functionalization with Ni of $Fe_{0.7}Cr_{1.3}O_3$/8YSZ electrode in a potentiometric sensor to selectively detect C_2H_4. *ACS Appl. Nano Mater.* **2018**, *1*, 6666–6673. [CrossRef]
42. Tewari, S.; Bhattacharjee, A. Structural, electrical and optical studies on spray-deposited aluminium-doped ZnO thin films. *Pramana* **2011**, *76*, 153–163. [CrossRef]
43. Gajdoš, M.; Eichler, A.; Hafner, J. CO adsorption on close-packed transition and noble metal surfaces: Trends from ab initio calculations. *J. Phys. Condens. Matter* **2004**, *16*, 1141–1164. [CrossRef]
44. Karczewski, J.; Bochentyn, B.; Molin, S.; Gazda, M.; Jasinski, P.; Kusz, B. Solid oxide fuel cells with Ni-infiltrated perovskite anode. *Solid State Ion.* **2012**, *221*, 11–14. [CrossRef]
45. Makgwane, P.R.; Ray, S.S. Nanosized ruthenium particles decorated carbon nanofibers as active catalysts for the oxidation of p-cymene by molecular oxygen. *J. Mol. Catal. A Chem.* **2013**, *373*, 1–11. [CrossRef]
46. Monteiro, N.; Noronha, F.; da Costa, L.; Linardi, M.; Fonseca, F. A direct ethanol anode for solid oxide fuel cell based on a chromite-manganite with catalytic ruthenium nanoparticles. *Int. J. Hydrogen Energy* **2012**, *37*, 9816–9829. [CrossRef]
47. Niranjan, R.; Sainkar, S.; Vijayamohanan, K.; Mulla, I. Ruthenium: Tin oxide thin film as a highly selective hydrocarbon sensor. *Sens. Actuators B Chem.* **2002**, *82*, 82–88. [CrossRef]
48. Pignat, K.; Vallotto, J.; Pinna, F.; Strukul, G. Cationic complexes of palladium (II) and platinum (II) as Lewis acid catalysts for the Diels−Alder reaction. *Organometallics* **2000**, *19*, 5160–5167. [CrossRef]
49. Dilonardo, E.; Penza, M.; Alvisi, M.; Cassano, G.; di Franco, C.; Palmisano, F.; Torsi, L.; Cioffi, N. Sensitive detection of hydrocarbon gases using electrochemically Pd-modified ZnO chemiresistors. *Beilstein J. Nanotechnol.* **2017**, *8*, 82–90. [CrossRef] [PubMed]
50. Ning, H.; Lan, Z.-Q.; Guo, J.; Tan, M.-Q. Carbon-monoxide adsorption and dissociation on Nb (110) surface. *Appl. Surf. Sci.* **2015**, *328*, 641–648. [CrossRef]
51. Chevallier, L.; di Bartolomeo, E.; Grilli, M.L.; Mainas, M.; White, B.; Wachsman, E.D.; Traversa, E. Non-Nernstian Planar Sensors Based on YSZ with a Nb2O5 Electrode. *Sens. Actuators B Chem.* **2008**, *129*, 591–598. [CrossRef]
52. Sekhar, P.K.; Subramaniyam, K. Electrical characterization of a mixed potential propylene sensor. *Sens. Actuators B Chem.* **2013**, *188*, 367–371. [CrossRef]
53. Liu, F.; Wang, B.; Yang, X.; Guan, Y.; Sun, R.; Wang, Q.; Liang, X.; Sun, P.; Lu, G. High-temperature stabilized zirconia-based sensors utilizing MNb_2O_6 (M: Co, Ni and Zn) sensing electrodes for detection of NO_2. *Sens. Actuators B Chem.* **2016**, *232*, 523–530. [CrossRef]
54. Romanytsia, I.; Viricelle, J.-P.; Vernoux, P.; Pijolat, C. Application of advanced morphology Au–X (X = YSZ, ZrO_2) composites as sensing electrode for solid state mixed-potential exhaust NO_x sensor. *Sens. Actuators B Chem.* **2015**, *207*, 391–397. [CrossRef]
55. Fergus, J.W. Perovskite oxides for semiconductor-based gas sensors. *Sens. Actuators B Chem.* **2007**, *123*, 1169–1179. [CrossRef]
56. Yamaguchi, M.; Anggraini, S.A.; Fujio, Y.; Sato, T.; Breedon, M.; Miura, N. Stabilized zirconia-based sensor utilizing SnO_2-based sensing electrode with an integrated Cr_2O_3 catalyst layer for sensitive and selective detection of hydrogen. *Int. J. Hydrogen Energy* **2013**, *38*, 305–312. [CrossRef]
57. Zosel, J. Response behavior of perovskites and Au/oxide composites as HC-electrodes in different combustibles. *Solid State Ion.* **2004**, *175*, 531–533. [CrossRef]
58. Park, C.O.; Fergus, J.; Miura, N.; Park, J.; Choi, A. Solid-state electrochemical gas sensors. *Ionics* **2009**, *15*, 261–284. [CrossRef]
59. Miura, N.; Raisen, T.; Lu, G.; Yamazoe, N. Highly selective CO sensor using stabilized zirconia and a couple of oxide electrodes. *Sens. Actuators B Chem.* **1998**, *47*, 84–91. [CrossRef]
60. Garzon, F. Solid-state mixed potential gas sensors: Theory, experiments and challenges. *Solid State Ion.* **2000**, *136–137*, 633–638. [CrossRef]
61. Miura, N.; Elumalai, P.; Plashnitsa, V.V.; Ueda, T.; Wama, R.; Utiyama, M. Solid-state electrochemical gas sensing. In *Solid State Gas Sensing*; Springer Science and Business Media LLC: Berlin/Heidelberg, Germany, 2009; pp. 1–27.
62. Wama, R.; Plashnitsa, V.V.; Elumalai, P.; Kawaguchi, T.; Fujio, Y.; Utiyama, M.; Miura, N. Improvement in propene sensing characteristics by the use of additives to In_2O_3 sensing electrode of mixed-potential-type zirconia sensor. *J. Electrochem. Soc.* **2009**, *156*, J102–J107. [CrossRef]

63. Sato, T.; Breedon, M.; Miura, N. Reduction in ethanol interference of zirconia-based sensor for selective detection of volatile organic compounds. *J. Electrochem. Soc.* **2013**, *160*, B146–B151. [CrossRef]
64. Ma, N.; Suematsu, K.; Yuasa, M.; Kida, T.; Shimanoe, K. Effect of water vapor on Pd-loaded SnO_2 nanoparticles gas sensor. *ACS Appl. Mater. Interfaces* **2015**, *7*, 5863–5869. [CrossRef] [PubMed]
65. Pal, N.; Murray, E. Dense $LaSrMnO_3$ composite electrodes for NO_x sensing. *Sens. Actuators B Chem.* **2018**, *256*, 351–358. [CrossRef]
66. Lee, D.; Ahn, S.-J.; Kim, J.; Moon, J. Influence of water vapor on performance of co-planar single chamber solid oxide fuel cells. *J. Power Sources* **2010**, *195*, 6504–6509. [CrossRef]
67. Adler, S.B. Factors governing oxygen reduction in solid oxide fuel cell cathodes. *Chem. Rev.* **2004**, *104*, 4791–4844. [CrossRef]
68. Baek, S.-W.; Jeong, J.; Schlegl, H.; Azad, A.; Park, D.S.; Baek, U.B.; Kim, J.H. Metal-supported SOFC with an aerosol deposited in-situ LSM and 8YSZ composite cathode. *Ceram. Int.* **2016**, *42*, 2402–2409. [CrossRef]
69. Lay, E.; Gauthier, G.; Dessemond, L. Preliminary studies of the Ba-doped La/Sr chromo-manganite series as new SOFC anode materials. *ECS Trans.* **2011**, *35*, 1345–1356. [CrossRef]